



CHORUS

This is the accepted manuscript made available via CHORUS. The article has been published as:

Reduced viscosity for flagella moving in a solution of long polymer chains

Yuchen Zhang, Gaojin Li, and Arezoo M. Ardekani

Phys. Rev. Fluids **3**, 023101 — Published 16 February 2018

DOI: [10.1103/PhysRevFluids.3.023101](https://doi.org/10.1103/PhysRevFluids.3.023101)

Reduced Viscosity for Flagella Moving in a Solution of Long Polymer Chains

Yuchen Zhang, Gaojin Li, and Arezoo M. Ardekani

School of Mechanical Engineering, Purdue University, West Lafayette, Indiana, 47906

The bacterial flagellum thickness is smaller than the radius of gyration of long polymer chains. The flow velocity gradient over the length of polymer chains can be non-uniform and continuum models of polymeric liquids break in this limit. In this work, we use Brownian Dynamics simulations to study a rotating helical flagellum in a polymer solution and overcome this limitation. As the polymer size increases, the viscosity experienced by the flagellum asymptotically reduces to the solvent viscosity. The polymer viscous stress for a solution of long polymer chains decreases with the inverse of polymer size to the power 1/2. The difference in viscosity experienced by the bacterial cell body and flagella can predict the non-monotonic swimming speed of bacteria in polymer solutions.

I. INTRODUCTION

The locomotion of microorganisms has been widely studied by experimentalists and theorists over the past fifty years [1–4]. The natural habitat of microorganisms often shows non-Newtonian behavior due to the presence of polymer molecules, proteins or other microstructures. Examples of microorganisms swimming in complex fluids include mammalian spermatozoa racing through cervical mucus in the female reproductive tract [5], the nematode *Caenorhabditis elegans* undulating its body to move through soil saturated with water [6], the ulcer-causing pathogen *Helicobacter pylori* releasing urease to swim through the gastric mucus [7], and Lyme disease spirochete *Borrelia burgdorferi* penetrating the extracellular matrix of the human skin [8].

Early experiments on a wide variety of flagellated bacteria have shown that a slight increase in the polymer concentration enhances the bacterial motility, whereas a further increase decreases it [9, 10]. Anisotropic elastic stresses [11–13] and shear thinning viscosity [14, 15] are considered as possible reasons for the speed enhancement. The elastic effects on various swimmers have been analyzed by using the Oldroyd-B model, which describes a dilute polymer solution of constant viscosity. The model predicts a velocity decrease for both infinite sheet and filament deformed by low-amplitude traveling waves [11, 16, 17], and a velocity increase for soft finite-length undulatory sheets with larger undulations at the tail [18, 19]. For helical flagella, the velocity enhancement due to elasticity is examined by Liu *et al.* [12], who measured the swimming speed of a force-free rotating helix in viscous and Boger (i.e., constant-viscosity elastic) fluids. The numerical simulation of a helical filament of a moderate thickness and pitch angle in an Oldroyd-B fluid also shows a modest speed enhancement for Deborah number on the order of $O(1)$ [13]. On the other hand, there is also a branch of studies that attribute the velocity enhancement to the shear-thinning viscosity of polymer solutions. The fluid near the flagellum is greatly deformed and exhibits a lower viscosity than the ambient fluids. The ambient fluids thus behave as a confinement, facilitating the swimming of the microorganism [14, 15].

In the case of the bacterial flagellum, a further examination of the dimension of the flagellum will cast doubt on the continuum concepts such as viscoelasticity and shear-thinning viscosity, because the flagellar thickness (~ 20 nm) can be smaller than the radius of gyration of polymer molecules (~ 60 nm) [20]. In an early experiment conducted by Berg and Turner [21], structured gel-like solutions containing long unbranched polymers (e.g., methylcellulose) hardly hindered the motility of tethered *E. coli*, while in homogeneous solutions containing branched polymers (e.g., Ficoll), the rotational rate of the cell body was the same as in the Newtonian fluid. They concluded that the micro-structure of polymers plays a key role in this case and the loose quasi-rigid polymer network is easier to be penetrated by particles of microscopic size. This argument is supported by the fact that the diffusion constant for small particles, or microscopic viscosity of a structured solution is lower than the apparent macroscopic viscosity. They also proposed that the network exerts forces normal to the segment of a moving slender body, enhancing the circumferential slip of helical flagella and generating more thrust. The idea of the enhancement in normal forces was then formulated into a mathematical model by Magariyama and Kudo [22]. In addition, Leshansky [23] modeled the propulsion of an undulating sheet in a sparse array of stationary obstacles that mimic the heterogeneous polymer network depicted by Berg and Turner. Stokesian dynamics simulations by Balin *et al.* [24] showed that the polymer molecules can migrate radially inward while being elongated by the flow.

Later, Martinez *et al.* [20] re-examined the argument by Berg and Turner and attributed the velocity enhancement of bacteria to the different viscosity experienced by the cell body and flagella. In their experiments, only the highest-molecular-weight polymer solutions led to an enhancement in the motility of *E. coli*, while the solutions containing lower molecular-weight polymers were described by Newtonian hydrodynamics. Based on the micro-rheology data for sub-micrometer beads, they concluded that the fast-rotating flagella see a lower viscosity than the cell body due to the shear thinning effects: the flagellum stretches the polymer coils into quasi-stationary objects, carving out a coil-sized channel void of polymers with viscosity approaching that of the solvent [20]. Recently, Patteson *et al.* found that the

long chain polymer solutions could suppress the tumbling motion of *E. coli* and enhanced its swimming speed [25]. By visualizing a single polymer, they suggested that the flow induced by *E. coli* effectively stretched the polymer molecules, and the elastic stress might be the reason of speed enhancement.

The Oldroyd-B model describes the constitutive equation for dilute polymer solutions, represented by short Hookean dumbbells in a homogeneous flow, i.e., the velocity gradient for all the dumbbells is constant [26, 27]. The model has been applied for many macroscopic hydrodynamic problems involving polymeric liquids. The use of Oldroyd-B model for the locomotion of helical flagella is, however, limited because the size of polymer coils can be comparable to the length scale over which the flow velocity gradient changes, i.e., the flagellum diameter.

In this article, the polymer molecules are studied in a coarse-grained manner to construct a microscopic picture of how polymer molecules are elongated near the flagella and how the polymer stress affects the motion of the flagellum. We used the Brownian Dynamics (BD) method to directly simulate the stochastic equation of dumbbells and overcome the limitations of continuum constitutive equations. The BD simulations are incorporated with the Stokes flow formulation of the distributed Lagrange multiplier method [28] to study the non-Newtonian effects on the locomotion of bacterial flagella. Here, we unravel the role of polymer chain length. For long polymer chains whose dimension is comparable to the flow length scale, the velocity experienced by each polymer molecule is non-homogeneous and this non-homogeneity can result in a reduced viscosity experienced by the flagellum.

II. NUMERICAL METHOD

II.1. Governing equations

In the simulation, the flagellum is modeled as an infinitely long helix rotating with a constant angular speed in a polymeric liquid. The polymer molecules are modeled as bead-spring dumbbells consisting of a spring connecting two beads that represent the ends of the polymer chain. Admittedly, the bead-spring dumbbell is a simplified model of polymer molecules since it doesn't include bending and twisting resistances. It can, however, capture the elastic nature of coiled linear polymer macromolecules [26]: the bead-spring dumbbell is a simplified model for the freely-jointed bead-rod chain (Kramers chain) that represents the coiled polymer chain. When the end-to-end vector of the Kramers chain is elongated, there will be a tension between the two ends to maintain the system entropy. This tension is represented by a spring connecting the beads. The spring is Hookean if the end-to-end vector of the Kramers chain is less than half of the contour length, otherwise, the spring approaches FENE (finitely extensible nonlinear elastic) [26]. A more accurate model of polymer molecules requires several dumbbells linked by extensional and angular (for bending resistance) springs, however, it significantly increases the complexity of the system.

The flow field is calculated from the three-dimensional incompressible Stokes equation with body forces added to the momentum equation to take into account hydrodynamic forces from the flagellum \mathbf{f}_f (calculated from distributed Lagrange multiplier method [15, 29]) and polymer beads \mathbf{f}_p (calculated from BD simulation [30, 31])

$$\rho \frac{\partial \mathbf{v}}{\partial t} = -\nabla p + \eta_s \nabla^2 \mathbf{v} + \mathbf{f}_f + \mathbf{f}_p, \quad \nabla \cdot \mathbf{v} = 0, \quad (1)$$

where \mathbf{v} is the background flow velocity, t is time, p is the hydrodynamic pressure, ρ and η_s are the density and viscosity of the solvent, respectively. A finite volume method based on a staggered grid is used to solve the background flow field on Eulerian grids. The flagellum and beads are discretized into Lagrangian points, denoted as \mathbf{x}_i and \mathbf{r}_j , respectively. The flow velocity on the Lagrangian points, denoted as \mathbf{v}_i for flagella and \mathbf{v}_j for beads, are interpolated from the background flow field \mathbf{v} .

$$\mathbf{v}_i = \int \delta(\mathbf{X} - \mathbf{x}_i) \mathbf{v}(\mathbf{X}) dV, \quad \mathbf{v}_j = \int \delta(\mathbf{X} - \mathbf{r}_j) \mathbf{v}(\mathbf{X}) dV, \quad (2)$$

where \mathbf{X} is the Eulerian coordinates, $\delta(\mathbf{X})$ is the discretized Dirac delta function, and dV is a differential volume element. The discretized Dirac delta function $\delta(\mathbf{X})$ is defined as [32]

$$\delta(\mathbf{x} - \mathbf{x}_i) = \phi_h\left(\frac{x - x_i}{\Delta x}\right) \phi_h\left(\frac{y - y_i}{\Delta y}\right) \phi_h\left(\frac{z - z_i}{\Delta z}\right) / \Delta x \Delta y \Delta z, \quad (3)$$

$$\phi_h(r) = \begin{cases} 1 - |r|, & \text{if } |\frac{x-x_i}{\Delta x}| < 1 \\ 0, & \text{otherwise,} \end{cases} \quad (4)$$

where $(\Delta x, \Delta y, \Delta z)$ is the grid spacing. After obtaining the flow field, the hydrodynamic force at the Lagrangian points of flagellum, denoted as \mathbf{F}_i , is calculated by satisfying the imposed kinematics of the helix by using a distributed Lagrange multiplier method [29, 33]. In each iteration \mathbf{F}_i is updated as

$$\mathbf{F}_i = \mathbf{F}_i^* + C_\alpha \frac{\rho V_i}{\Delta t} (\mathbf{U} + \boldsymbol{\omega}_p \times \mathbf{x}_i + \mathbf{v}_s - \mathbf{v}_i), \quad (5)$$

$$\mathbf{U} = \frac{1}{M_p} \int_{V_p} \rho (\mathbf{v}_i - \mathbf{v}_s) dV, \quad (6)$$

$$\boldsymbol{\omega}_p = \frac{1}{I_p} \int_{V_p} \rho \mathbf{x}_i \times (\mathbf{v}_i - \mathbf{v}_s) dV, \quad (7)$$

where \mathbf{F}_i^* is the force calculated in the previous iteration, C_α is a dimensionless factor whose value affects the convergence rate but not the solution, V_i is the volume of the Lagrangian grid cell, Δt is the time step size, \mathbf{v}_s is the imposed velocity, V_p , M_p and I_p are the volume, mass and moment of inertia of the flagellum, respectively. Flagellum density is assumed to be the same as the background fluid density. For constant ρ and C_α , the above mentioned equations satisfy the force-free and torque-free conditions. For rotating flagella with a constant angular speed, Eq. (7) is not needed since $\boldsymbol{\omega}_p$ is equal to the imposed angular speed. In this case, the flagellum is force-free but not torque-free.

The motion of each bead is governed by the following stochastic equation, where inertia and excluded volume are neglected

$$d\mathbf{r}_j = [\mathbf{v}_j + \frac{\mathbf{F}_j^e}{\zeta}] dt + \sqrt{\frac{2k_B T}{\zeta}} d\mathbf{W}_j, \quad (8)$$

where $\zeta = 6\pi\eta_s r_b$ is the Stokes drag coefficient with r_b being the radius of beads, k_B is the Boltzmann constant, T is the absolute temperature, $d\mathbf{W}_j$ is the three-dimensional Gaussian white noise vector with each component represented by a Gaussian random number with zero mean and a variance of dt , and \mathbf{F}_j^e is the elastic force of springs, which follows finitely extensible nonlinear elastic (FENE) law, $\mathbf{F}_i^e = H\mathbf{Q}/(1 - Q^2/Q_m^2)$, where H is the spring stiffness in the absence of shear, $\mathbf{Q} = \mathbf{r}_{j+1} - \mathbf{r}_j$ is the connector vector of springs with its magnitude denoted as Q , Q_m is the maximum length of each spring. The extensibility parameter of dumbbells is defined as $\tilde{b} = HQ_m^2/k_B T$. Unless otherwise stated, Hookean dumbbells are used corresponding to $\tilde{b} \rightarrow \infty$. At each time step, Eq.(8) is iteratively solved. $d\mathbf{W}_j$ changes with time but is constant at each iteration. By using the position of beads in the previous iteration \mathbf{r}_j^n , the spring force \mathbf{F}_j^e and the flow velocity \mathbf{v}_j are obtained and then used to calculate the new position of beads \mathbf{r}_j^{n+1} .

Finally, the flow velocity is calculated again by using Eq.(1). Here, the body force from the flagellum \mathbf{f}_f is extrapolated from the hydrodynamic force exerted on the Lagrangian grids of flagellum \mathbf{F}_i . The body force from spring dumbbells \mathbf{f}_p is extrapolated from the elastic force \mathbf{F}_j^e at the position of beads \mathbf{r}_j .

$$\mathbf{f}_f(\mathbf{X}) = \sum_i \delta(\mathbf{X} - \mathbf{x}_i) \mathbf{F}_i, \quad \mathbf{f}_p(\mathbf{X}) = \sum_j \delta(\mathbf{X} - \mathbf{r}_j) \mathbf{F}_j^e, \quad (9)$$

In the simulation, \mathbf{f}_f , \mathbf{f}_p , and \mathbf{v} are correlated, Table I shows a summary of above mentioned steps.

TABLE I. Iterative schemes for the distributed Lagrange multiplier method coupled with implicit BD simulatons.

Compute the flow field using Eq.(1) with initial guess of \mathbf{f}_p and \mathbf{f}_f as $\mathbf{0}$.
Calculate the body forces exerted by the flagellum \mathbf{f}_f : Interpolate the flow velocity \mathbf{v} on Lagrangian points of the flagellum as \mathbf{v}_i (Eq.(2)) Calculate the hydrodynamic force \mathbf{F}_i at Lagrangian points of flagellum by using Eq.(5) Extrapolate \mathbf{F}_i on the Eulerian grids by using Eq.(9)
Calculate the body forces of beads \mathbf{f}_b : Interpolate the flow velocity \mathbf{v} at j-th bead \mathbf{r}_j^n as \mathbf{v}_j (Eq.(2)) Calculate the spring force on the bead as \mathbf{F}_j^e Evaluate the new position of each bead \mathbf{r}_j^{n+1} by using Eq.(8). Extrapolate spring forces \mathbf{F}_j^e on the Eulerian grids by using Eq.(9)
Recalculate the flow field

II.2. Problem Setup

Each material point on the helix that is swimming in the positive x-direction follows

$$\mathbf{x}(s, t) = (\alpha s + Ut)\hat{\mathbf{x}} + R_h[\cos(ks + \omega t)\hat{\mathbf{y}} + \sin(ks + \omega t)\hat{\mathbf{z}}], \quad (10)$$

where s is the arc length, U is the swimming speed, k is the wave number measured on the arc length of the helix, ω is the angular speed, $\alpha = \cos(\phi)$ with $\phi = 0.27\pi$ being the pitch angle, and $R_h = \sin(\phi)/k$ is the helical radius. Only one period of the helix is studied in the simulation and periodic boundary conditions are used in the x-direction. At boundaries in y and z directions, $\partial u/\partial y$ and $\partial u/\partial z$ are set to zero.

Unless otherwise stated, the reported variables in simulations of flagella are scaled as follows: the length is scaled by $1/k$, velocity by ω/k , and time by $1/\omega$. The simulation domain is $2\pi \cos(\phi) \times 20 \times 20$, and is resolved using two different mesh patterns. Uniform fine mesh is used inside a $2\pi \cos(\phi) \times 5.0 \times 5.0$ rectangular block in the middle of the domain with grid spacing $\Delta x = \Delta y = \Delta z = \pi \cos(\phi)/64$. The simulation results are independent of the size of this block. Outside this block, grid spacing in y and z directions are elongated and the domain is resolved using $128 \times 26 \times 26$ grids. The helix is resolved using 200 circles that are perpendicular to the helical center line and each circle is discretized by 6 grid points. The radius of the circle is $r_f = 0.001$. A total of 4 million dumbbells are initialized within a cylinder around the helix. The radius of the cylinder is 2.4 and the dumbbells are initially uniformly distributed in space. The length vector of Hookean dumbbells \mathbf{Q} initially follows the Gaussian distribution with variance of $k_B T/H$ for each component. For FENE dumbbells, the initial length is set to be constant, $Q = \sqrt{3k_B T/H}$.

II.3. Polymer solution rheology and dimensionless parameters

The apparent viscosity and relaxation time of the polymer solution can be determined based on the parameters of dumbbells. The relaxation time of polymer molecules (in quiescent fluids) is defined by the relaxation time of Hookean dumbbells $\lambda_H = \zeta/4H$. The apparent polymer viscosity is $\eta_p = n_p k_B T \lambda_H$, where n_p is the average number density of dumbbells. The mean-squared radius of gyration can be calculated from Kramers chain model $\langle R_g^2 \rangle = \langle Q^2 \rangle_0/6$ [26]. Polymer solutions with the shear-thinning viscosity is represented by FENE dumbbells with a finite extensibility parameter \tilde{b} . A smaller \tilde{b} corresponds to stronger shear-thinning effects.

The important dimensionless numbers in BD simulations of a rotating helix are: Deborah number $De = \lambda_H \omega$, Gradient number $Gd = \sqrt{\langle Q^2 \rangle_0} k$, and viscosity ratio between the polymer and the solvent $\gamma = \eta_p/\eta_s$. The Deborah number is the ratio of the relaxation time of dumbbells over the characteristic time scale of the background flow. The Gradient number is the ratio of the mean-squared dumbbell length $\sqrt{\langle Q^2 \rangle_0} = \sqrt{c k_B T/H}$ over the characteristic length of the flow $L = 1/k$ [34], where $\langle \dots \rangle$ denotes the ensemble average, subscript ‘‘0’’ means that the average is evaluated in a quiescent fluid, and $c = 3$ is the number of dimensions. The Péclet number is defined as $Pe = \omega L^2/D_{tr}$, where $D_{tr} = k_B T/2\zeta$ is the translational diffusivity of dumbbells. The Péclet number can be evaluated based on De and Gd as $Pe = 8cDe/Gd^2$.

The polymer stress is calculated by using the Kramers-Kirkwood form of the stress tensor and is then normalized by $\eta_p \omega = n_p k_B T \lambda_H \omega$

$$\boldsymbol{\tau}_p = \frac{\tilde{\boldsymbol{\tau}}_p}{n_p k_B T \lambda_H \omega}, \quad \tilde{\boldsymbol{\tau}}_p = \langle \mathbf{Q} \mathbf{F}_j^e \rangle - n_p k_B T \boldsymbol{\delta}. \quad (11)$$

For Hookean dumbbells, the above equation simplifies to $\boldsymbol{\tau}_p = \tilde{\boldsymbol{\tau}}_p/\eta_p \omega = (3\langle \mathbf{Q} \mathbf{Q} \rangle / \langle Q^2 \rangle_0 - \boldsymbol{\delta})/De$ and $tr(\boldsymbol{\tau}_p)$ represents the dimensionless polymer distension, where $\boldsymbol{\delta}$ is the identity tensor. The position of dumbbells is defined at their mid point. To reduce the noise in the results, we exploited the helical symmetry and converted all the dumbbell onto the same plane perpendicular to the axis of the helix. The plane is divided into small bins of size $l = 0.02$ and the components of $\mathbf{Q} \mathbf{F}_j^e$ are summed for all the dumbbells inside each bin. The number density of dumbbells for each bin is also calculated and normalized by the average number density of dumbbells n_p .

II.4. Comparison to an Oldroyd-B fluid

The locomotion of the flagellum in an Oldroyd-B fluid is quantified to compare the results against the BD simulation results in the limit of small dumbbell length (small Gd). Here, the elastic and viscous stresses splitting (EVSS) method

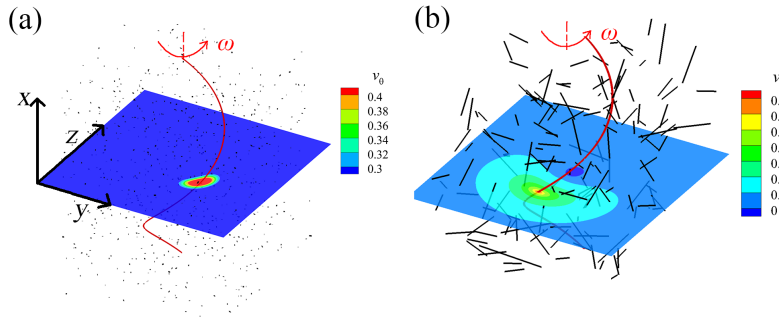


FIG. 1. The schematic of the Brownian Dynamic simulation for (a) short ($Gd=0.0055$) and (b) long ($Gd=0.55$) polymer chains in the flow induced by the flagellum. The kinetics of dumbbells leads to the Oldroyd-B model if the velocity gradient experienced by polymer chains is assumed to be constant, which is not the case for bacterial flagella in solutions of long polymer chains and the Brownian Dynamic simulation is required. In Fig. (a), polymer dimension is very small compared to the flow length scale, the velocity gradient over the length of dumbbell is almost uniform, and the BD model recovers the Oldroyd-B equation. However, when polymer dimension is comparable to the flow length scale in Fig. (b), the non-homogeneous effects become important, causing the BD simulation to deviate from the Oldroyd-B model. Here, the pitch angle is $\phi = 0.27\pi$. The filament radius is very small $r_f = 10^{-3}$, and $\gamma = \eta_p/\eta_s = 0$.

[35] is applied. The main difference between the Oldroyd-B and BD simulations is the calculation of \mathbf{f}_p in Eq. (1). In an Oldroyd-B fluid,

$$\mathbf{f}_p = \nabla \cdot \tilde{\boldsymbol{\tau}}_p, \quad \tilde{\boldsymbol{\tau}}_p + \lambda_H \overset{\nabla}{\tilde{\boldsymbol{\tau}}}_p = \eta_p \mathbf{D}, \quad (12)$$

where $\mathbf{D} = \nabla \mathbf{v} + \nabla \mathbf{v}^T$ is the rate of strain tensor, and the notation $\overset{\nabla}{\tilde{\boldsymbol{\tau}}}_p$ represents the upper-convected derivative of $\tilde{\boldsymbol{\tau}}_p$. The Oldroyd-B constitutive equation is solved explicitly, requiring a smaller time step compared to BD simulations. The results of Oldroyd-B and BD simulations are independent of time step. The normalized time step size is 0.02 and 0.0025 for BD and Oldroyd-B simulations, respectively. The mesh independence test has been performed, and the maximum error for the swimming speed in a Newtonian fluid is 1.2% for mesh size $\Delta x = \Delta y = \Delta z = \pi \cos(\phi)/64$.

The Oldroyd-B model describes the kinetics of Hookean dumbbells when (a) the hydrodynamic interactions between beads and boundaries (i.e., flagellum in our simulations), and between beads themselves are negligible, (b) the dumbbell length (i.e., Gd) is very small, and (c) dumbbells are exposed to a homogeneous flow (i.e., velocity gradient is constant). For very small polymer viscosity γ , condition (a) is satisfied. Hydrodynamic interactions between the beads and flagellum and between beads themselves are included in our BD simulations. The flagellum is very thin so that the hydrodynamic interaction between beads and the flagellum is negligible. The motion of the flagellum is mainly influenced by the polymer stress in its vicinity. When the swimming speed of the flagellum reaches the steady state, the dumbbells near the flagellum are greatly stretched and the hydrodynamic interaction between beads is negligible [36]. Therefore, for a wide range of polymer viscosity ratio, condition (a) is satisfied.

The BD simulation mainly differs from the Oldroyd-B model in that the flow velocity of polymer molecules is non-homogeneous. The kinetics of Hookean dumbbells leads to the Oldroyd-B model only if the velocity gradient is assumed to be constant, while in our BD simulations, the velocity gradient experienced by a dumbbell depends on its position and length. Due to this nonhomogeneous effect, the BD results can only recover the Oldroyd-B results for small Deborah numbers. The following constitutive equations take into account of the position dependence of velocity gradient and can describe the kinetics of short Hookean dumbbells in a non-homogeneous flow in the limit of small Gd (i.e., large Pe) [27]

$$Pe \frac{Dn}{Dt} = \nabla^2 n - 2De^2 \nabla \nabla : (\boldsymbol{\tau}_p \cdot \nabla \mathbf{v}) + 2De \nabla \nabla : (n \nabla \mathbf{v}) + De \nabla \nabla : \boldsymbol{\tau}_p, \quad (13)$$

$$\boldsymbol{\tau}_p + De \overset{\nabla}{\boldsymbol{\tau}}_p - \frac{De}{Pe} \nabla^2 \boldsymbol{\tau}_p + 2 \frac{De^2}{Pe} \nabla \nabla : (\boldsymbol{\tau}_p \cdot \nabla \mathbf{v}) \boldsymbol{\delta} - 2 \frac{De}{Pe} \nabla \nabla : (n \nabla \mathbf{v}) \boldsymbol{\delta} - \frac{De}{Pe} (\nabla \nabla : \boldsymbol{\tau}_p) \boldsymbol{\delta} = -n \mathbf{D}, \quad (14)$$

where n is the number density of dumbbells. At infinitely large Pe , Eq. (13) leads to $Dn/Dt = 0$, the polymer concentration remains uniform at the quasi-steady state, and the stress equation Eq. (14) recovers the Oldroyd-B constitutive equation. By comparing Eq. (14) with the Oldroyd-B constitutive equation (Eq. (12)), we see that terms

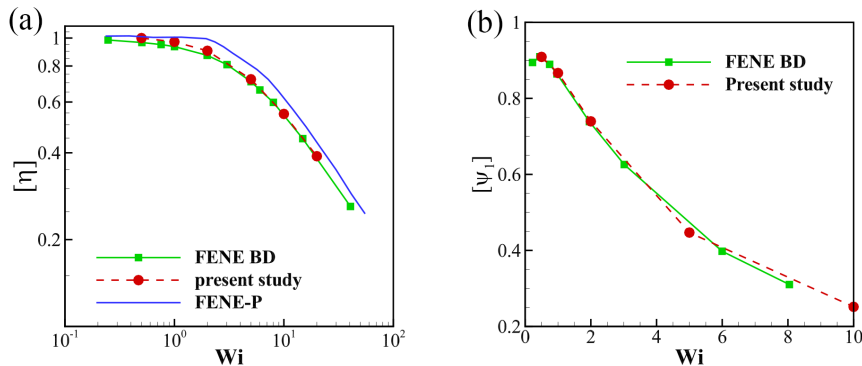


FIG. 2. (a) Shear rate dependence of the normalized viscosity of FENE dumbbells (BD simulation results by Rudisill and Cummings [36] and the present study) and FENE-P dumbbells (analytical solutions of Bird *et al.* [37]). (b) Strain rate dependence of the normalized first normal stress coefficient of FENE dumbbells by Rudisill and Cummings [36] and this work. The extensibility parameter of FENE dumbbells is $\tilde{b} = 100$. The results do not include hydrodynamic interactions and excluded volume for polymer molecules.

due to non-homogeneity of velocity gradient are on the order of $De^2/Pe \sim Gd^2De$. Thus, only for small values of Gd and De , the results of BD simulations are in agreement with those of the Oldroyd-B fluid.

By setting $Dn/Dt = 0$ in Eq. (13), we can get the steady-state concentration of polymer molecules in a non-homogeneous flow, which is not uniform and only depends on De . For an Oldroyd-B fluid, this steady state distribution cannot be reached in practice because it requires an infinitely long time. The time scale of polymer migration is proportional to the Péclet number. For very small Gd (or large Pe), the migration of polymer molecules is so slow that their concentration is almost uniform at the finish time of our simulations. In our BD simulations, the polymer molecules are stretched in a relatively short time, and the swimming speed of the flagellum rapidly changes. After reaching the quasi-steady state where the polymer molecules are fully stretched, the swimming speed can still slightly change due to the polymer migration, which takes a very long time. The results are evaluated at the quasi-steady state, where polymer molecules are fully stretched.

III. VALIDATION OF THE NUMERICAL METHOD

III.1. Case A: FENE dumbbells in a simple shear flow

To validate our BD simulations, the intrinsic viscosity and the first normal stress coefficient of FENE dumbbells in a simple shear flow are compared against BD simulation results of Rudisill and Cummings [36] in Fig. 2. Here, the polymer viscosity η_p is very small, so that the background flow field is not affected by the elastic stresses of dumbbells and recovers the Newtonian solution $\mathbf{v} = \dot{\gamma}y\hat{x}$, where $\dot{\gamma}$ is the shear rate. Meanwhile, the dilute assumption is satisfied so that the hydrodynamic interaction between the beads and boundaries and between beads themselves are negligible. The Weissenberg number is $Wi = \lambda_H \dot{\gamma}$. The viscosity and first normal stress coefficient are calculated and scaled as [36]

$$[\eta] = \frac{\eta_p}{n_p k_B T \lambda_H}, \quad \eta_p = n_p \langle Q_x F_y^e \rangle / \dot{\gamma}, \quad (15)$$

$$[\Psi_1] = \frac{\Psi_1}{2n_p k_B T \lambda_H^2}, \quad \Psi_1 = n_p [\langle Q_x F_x^e \rangle - \langle Q_y F_y^e \rangle] / \dot{\gamma}^2. \quad (16)$$

The intrinsic viscosity and first normal stress coefficient of our BD simulation results are in good agreement with that of Rudisill and Cummings [36]. In Fig. 2(a), the analytical solution of FENE-P dumbbells is also included. The elastic force of FENE-P dumbbells is $\mathbf{F}_i^e = H\mathbf{Q}/(1 - \langle Q^2 \rangle / Q_m^2)$.

III.2. Case B: A two-dimensional undulating swimming sheet

Before we study the helical flagellum, we validate BD results for a two-dimensional undulating sheet against the results in an Oldroyd-B fluid for a very small Gradient number. The parameters are scaled in the same way as the

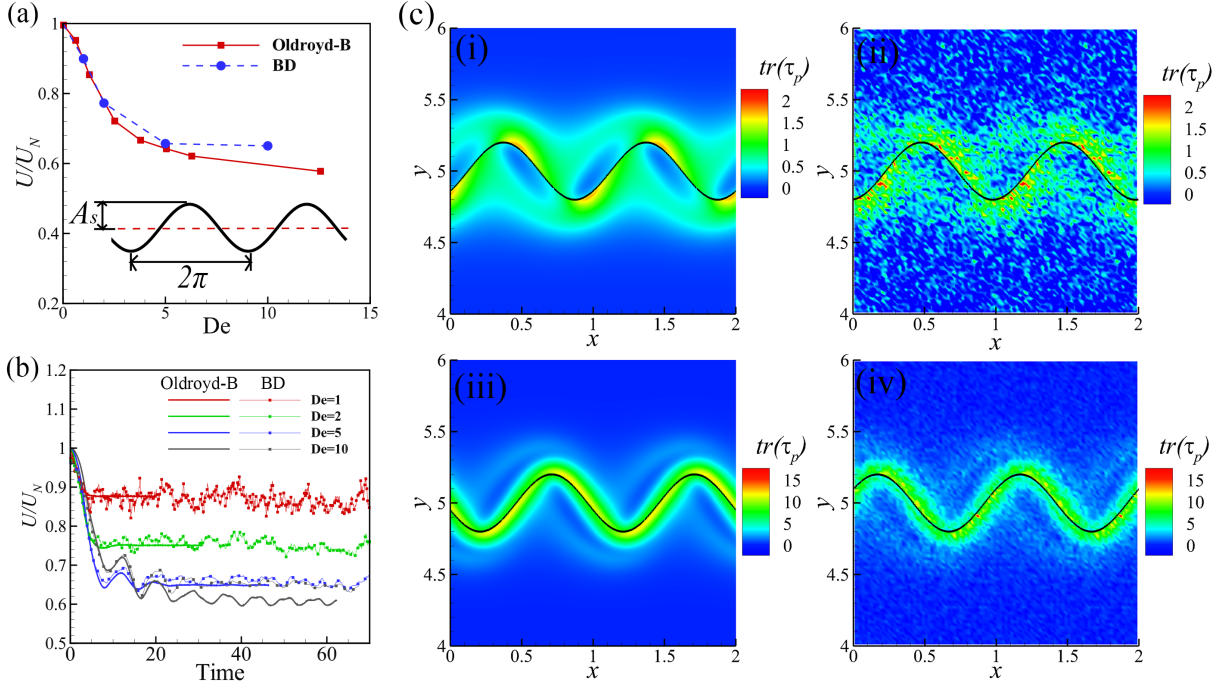


FIG. 3. (a) The quasi-steady state swimming speed of an undulating sheet at different Deborah numbers using the Oldroyd-B constitutive equation and BD simulations. The results are normalized by the swimming speed in the Newtonian fluid. Here, the dumbbell length is very small ($Gd=0.089$). The BD result matches the Oldroyd-B result for small De , and deviate from it at large De due to the flow inhomogeneity effect, which is on an order of Gd^2De . (b) The corresponding temporal evolution of swimming speed for the study in Fig. (a). The BD results quantitatively match Oldroyd-B results. (c) Comparison of the normalized polymer distention $tr(\tau_p)$ at $De=1.0$ for (i) the Oldroyd-B fluid and (ii) the BD simulations, and at $De=5.0$ for (iii) the Oldroyd-B fluid and (iv) the BD simulations.

simulation of the helical flagellum, and the wave number k is equal to 2π over one wavelength of the sheet. Only one period of oscillation is included in the computational domain. Periodic boundary conditions are applied in the x -direction. The sheet has a very small thickness $t_s = 0.02\pi$ with an amplitude of oscillation $A_s = 0.4\pi$. The simulation domain is 1×10 , where 256×666 grid points are used to resolve an 1×2.6 domain around the sheet, and 256×234 to resolve the outer coarser domain. The simulation parameters are number of dumbbells $N = 5 \times 10^5$, $Re = \rho\omega/\eta_s k^2 = 4.8 \times 10^{-5}$, $\gamma = \eta_p/\eta_s = 1$, $Gd = 0.089$.

Fig. 3(a) illustrates that the swimming speed at the quasi-steady state computed from BD simulations is in agreement with Oldroyd-B results for small Deborah numbers. Due to small values of Gd , the polymer concentration here is almost uniform. Although there are noises due to the stochastic nature of BD simulations, the temporal evolution of swimming speed also follows the same trend as the one in the Oldroyd-B fluid (Fig. 3(b)). At higher De , BD results deviate from those of Oldroyd-B fluids due to the inhomogeneity of velocity gradient, which is on the order of Gd^2De [27]. In Fig. 3(c), the trace of polymer stress $tr(\tau_p)$, which corresponds to the polymer distention and the elastic energy stored in Hookean dumbbells, is in good agreement with the Oldroyd-B results. As Deborah number increases, the elastic stress increases and becomes more concentrated near the sheet.

IV. RESULTS

IV.1. Rotating flagellum in polymeric solutions

The swimming speed and torque of a force-free flagellum that rotates with a constant angular speed and is immersed in short polymer solutions (very small Gd) are shown in Fig. 4(b). Similarly to the conclusion drawn for the 2D undulating sheet, the BD results agree with the Oldroyd-B fluid at low Deborah numbers and deviate from it for larger De due to flow inhomogeneity effects, which is on the order of Gd^2De [27]. Here, both BD and Oldroyd-B simulations show a decreasing velocity and increasing torque for an increasing fluid elasticity. The temporal evolution

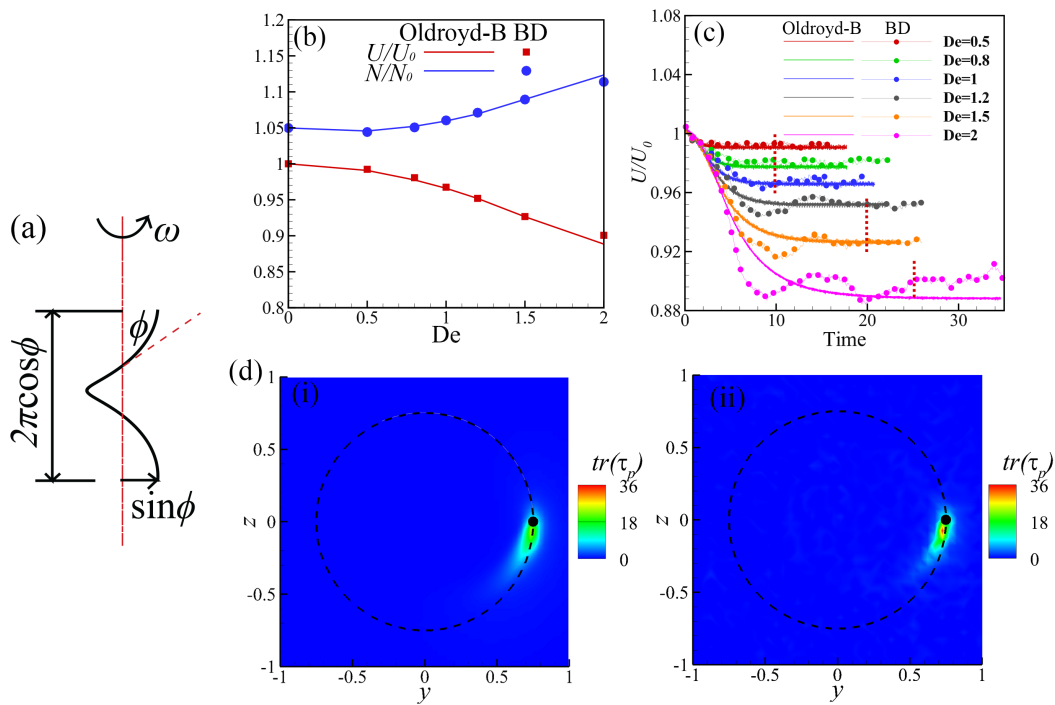


FIG. 4. (a) Schematic of the helical flagellum. (b) The swimming speed U/U_0 and torque N/N_0 normalized by the results in the solvent computed from BD and Oldroyd-B simulations for very short polymer chains. (b) The time evolution for the swimming velocity. The quasi-steady state results in Fig.(b) are evaluated as the average normalized velocity after the time marked by red dashed lines. (d) The trace of polymer stresses at $De=0.5$ for (i) Oldroyd-B results and (ii) BD results are also in good agreement. The cross section of the helix denoted by the black dot $(\sin(\phi), 0)$ is rotating around $(0, 0)$ along the dashed circle. Here, the pitch angle is $\phi = 0.27\pi$. The filament radius is very small $r_f = 10^{-3}$, $\gamma = \eta_p/\eta_s = 0.05$, $Gd = 0.0055$.

of swimming speed from BD simulations is also compared with the Oldroyd-B results in Fig. 4(c). Because the Reynolds number in the simulation is very small, the swimming speed increases from zero to the Newtonian speed in a very short period of time, which is not discernible in the figure. As the polymer molecules are stretched, the swimming velocity decreases. The swimming speed of BD simulations deviates from the Oldroyd-B results at the beginning of the simulation, but then reaches the same quasi-steady state. The deviation is due to the fact that when dumbbells are very short, the hydrodynamic interaction between beads are important, which is present in the BD simulation but not in the Oldroyd-B fluid. The initial dumbbell length is very small here due to the very small Gradient number used in this case. As the polymer molecules are stretched by the rotating helix, the hydrodynamic interaction between beads decreases and the swimming speed of the helix reaches the same quasi-steady state as the Oldroyd-B fluid. However, when De exceeds 1.5, the quasi-steady state swimming speed of BD simulations deviates from the Oldroyd-B results due to the non-homogeneity in the velocity gradient. The deviation occurs at a lower Deborah number than an undulating sheet, because the velocity gradient of the helix changes more rapidly. In Fig. 4(d), the mean-squared distension field computed from the BD simulation is in good agreement with Oldroyd-B results. The simulation parameters are $Re = \rho\omega/\eta_s k^2 = 9.42 \times 10^{-3}$, $\gamma = \eta_p/\eta_s = 0.05$, $Gd = 0.0055$.

By using the BD simulations, we are able to explore the role of rheological properties of polymers whose dimension is comparable to the flow length scale. Fig. 5(a) shows the polymer length (Gd) dependence of the swimming speed and torque for the helical flagellum. The hydrodynamics of the flagellum is independent of Gd for small polymer sizes, but when the polymer size exceeds a threshold value, the free-swimming velocity U of the flagellum approaches that in the Newtonian fluid, and the torque acting on the flagellum asymptotically decreases to that in the pure solvent. For the bacterium *E. coli*, its flagellum typically has one pitch of $2\pi/k \approx 2.5 \mu\text{m}$, pitch angle of $\phi \approx 0.22\pi$ and filament diameter of 20 nm [38]. The velocity enhancement is experimentally observed for flagella rotating with an angular speed of $\omega \approx 700 \text{ rad/s}$ in a polymer solution with radius of gyration $R_g = 56 \text{ nm}$ and relaxation time $\lambda \sim 1 \text{ ms}$ [20]. The dimensionless numbers for this polymer solution are $De \approx 0.7$ and $Gd \approx 0.34$. The black dot in Fig. 5(a) indicates the normalized torque at this Gd , which is lower than $1 + \gamma$, implying that the local viscosity experienced by the flagellum is lower than the apparent viscosity of the polymer solution. This agrees with the experimental findings by Martinez *et al.* [20] that the viscosity experienced by the flagellum is close to the solvent viscosity rather than the

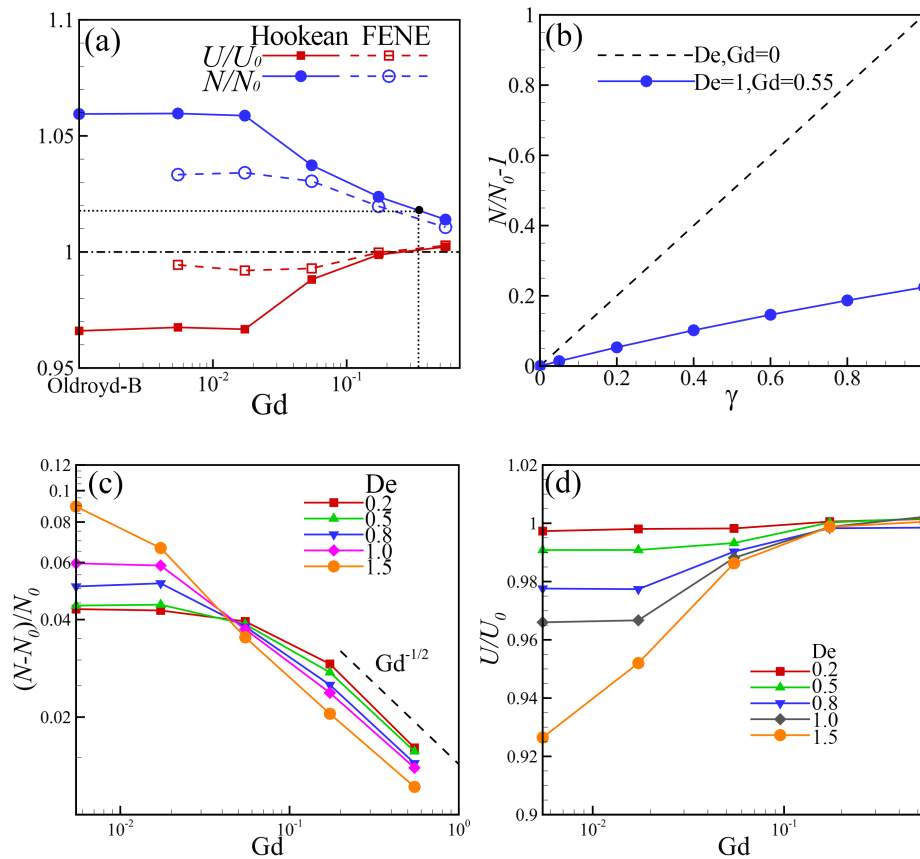


FIG. 5. (a) The role of polymer size, i.e., Gradient number, on the normalized swimming speed and torque of the helix at $De=1.0$. The black dotted line illustrates the torque for the flagellum of *E. coli*. The viscosity experienced by the flagellum is closer to the solvent viscosity (1.0) than the apparent viscosity ($1 + \gamma$). (b) The normalized torque difference between the polymer solution and the solvent, corresponding to the microscopic viscosity contributed by polymer molecules, is proportional to the polymer viscosity ratio γ . The viscosity contributed by polymer molecules are closer to 0 than the apparent polymer viscosity γ , which is illustrated by the dashed line. Here, $Gd=0.55$ (c) The Gradient number dependence of the torque difference between the polymer solution and the solvent, or the microscopic viscosity contributed by the polymer molecules. At large Gd, this viscosity decreases as $Gd^{-1/2}$. (d) the Gradient number dependence of the swimming speed for different De. At large Gd, the polymer elastic stress is negligible and the swimming speed approaches that in Newtonian fluids. Here, $\phi = 0.27\pi, \gamma = 0.05$, and $r_f = 10^{-3}$.

apparent viscosity. Here, we showed a relatively small reduction of microscopic viscosity because the polymer viscosity ratio γ is small. As is shown in Fig 5(b), the viscosity contributed by the polymer molecules, which is measured as the torque difference between the polymer solution and the solvent ($N/N_0 - 1$), is proportional to the viscosity ratio γ . For polymer solutions of higher concentration, there will be a large viscosity reduction from the apparent polymer viscosity.

Fig. 5(c) shows the normalized torque difference between the solution and the solvent, or the viscosity contributed by the polymer molecules for different De and Gd. This viscosity is constant for small Gradient numbers and then decreases with Gd beyond a threshold. The critical Gd, at which the polymer viscosity start vanishing, decreases with Deborah number. At large Gd, the polymer viscosity, or the polymer viscous stress, decreases as $Gd^{-1/2}$. The corresponding swimming speed is shown in Fig. 5(d). At large Gd, Deborah number and polymer elastic effects are not important, and the swimming speed of the flagellum approaches that in the pure solvent.

The spring in the dumbbell models the tension caused by the entropy change when the polymer chain is stretched. The spring stiffness reduces for longer polymer chains, and the corresponding dumbbell is stretched by Brownian motion to a larger mean-squared length in quiescent fluids. When polymer dimension is very small compared to the flow length scale, the velocity gradient over the length of dumbbells is uniform and the kinetics of the dumbbells recovers the Oldroyd-B constitutive equation, indicating that the polymer stress is only dependent on the Deborah number but independent of Gd. On the other hand, if the polymer dimension is comparable to the flow length scale, the velocity gradient over the dumbbell is not uniform. The velocity difference for the two ends of the dumbbell

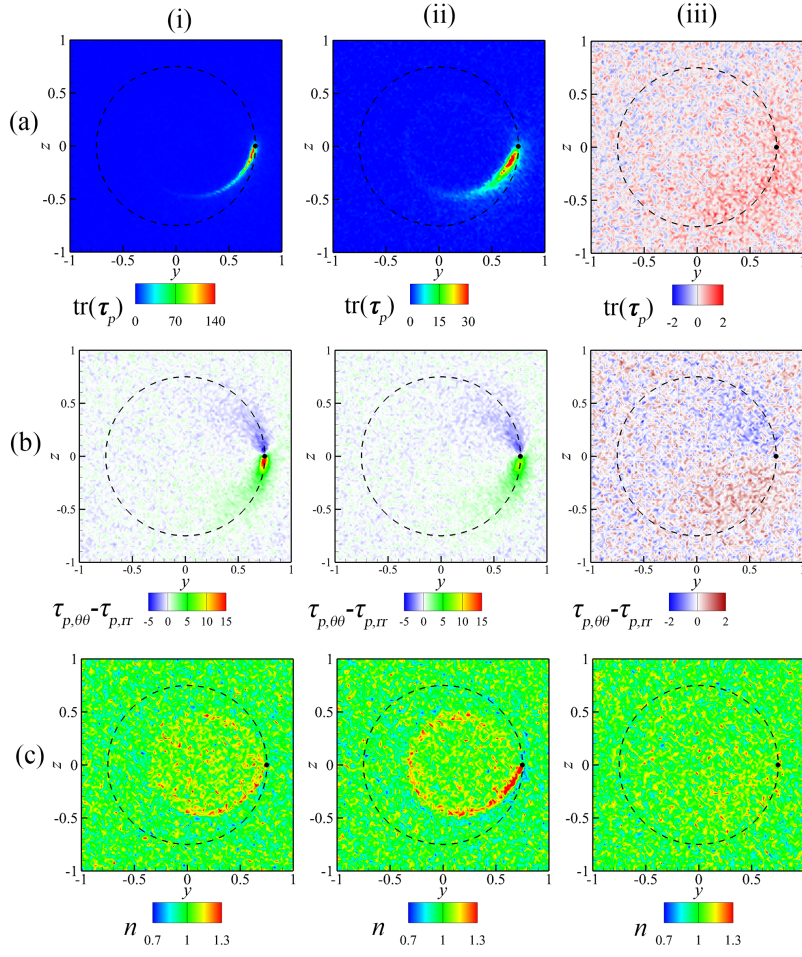


FIG. 6. (a) The normalized polymer distension $tr(\tau_p)$ at $De=1.0$, (b) the first normal stress difference $\tau_{p,\theta\theta} - \tau_{p,rr}$ at $De=0.2$ and (c) the polymer number density at $De=1$ for Gradient numbers (i) 0.0055, (ii) 0.055, and (iii) 0.55. The results are the spatial averaged values along the center line of the helix. Here, $\phi = 0.27\pi, \gamma = 0.05$, and $r_f = 10^{-3}$.

cannot exceed the velocity of the flagellum segment. Thus, longer polymer chains tend to experience a smaller averaged velocity gradient over their lengths, exerting less polymer stresses. The reduction of the polymer stress begins when dumbbell length Q is larger than the length scale over which the flow velocity gradient changes. When Deborah number increases, polymer chains are stretched to a larger length compared to that in quiescent fluids, i.e., $Q^2/\langle Q^2 \rangle_0$ is larger. Therefore, the critical Gd, which is related with $\langle Q^2 \rangle_0$, decreases with Deborah number. Another possible reason for the reduction of polymer stress is the reduced polymer stretching time. A larger Gradient number indicates a smaller Pe, thus the polymer molecules have a larger length scale of Brownian motion compared to the length scale of the flow. Driven by the stronger Brownian motion, the segments of polymer molecules are more likely to escape from the vicinity of flagellum and the flagellum can only stretch the polymer molecules for a smaller period of time.

The contour plots of polymer stress and the number density are shown in Fig. 6. Here, we used the normalized polymer distension (Fig. 6(a)) to evaluate the polymer elastic stress and the normal stress difference at small De (Fig. 6(b)) to evaluate the polymer viscous stress, because the polymer viscous stress $\eta_p(\nabla \mathbf{v} + \nabla \mathbf{v}^T)$, whose trace is zero, does not contribute to the polymer distension $tr(\tau_p)$, but contributes to the normal stress difference $(\tau_{p,\theta\theta} - \tau_{p,rr})$. From the contour plots, both polymer viscous and elastic stresses decrease with Gd in a non-homogeneous regime. A mild polymer migration is observed in Fig. 6(c), but it hardly affects the torque and swimming speed of the rotating helix. The polymer migration increases with Gd first and then decreases. Eq. (13) describes variation of number density for very short Hookean dumbbells and suggests that in the limit of small Gd, the rate of change of number density is proportional to Pe^{-1} , i.e., Gd^2 . But when Gd further increases, this constitutive equation is no longer applicable. The polymer stress decreases and the stress-induced polymer migration becomes negligible.

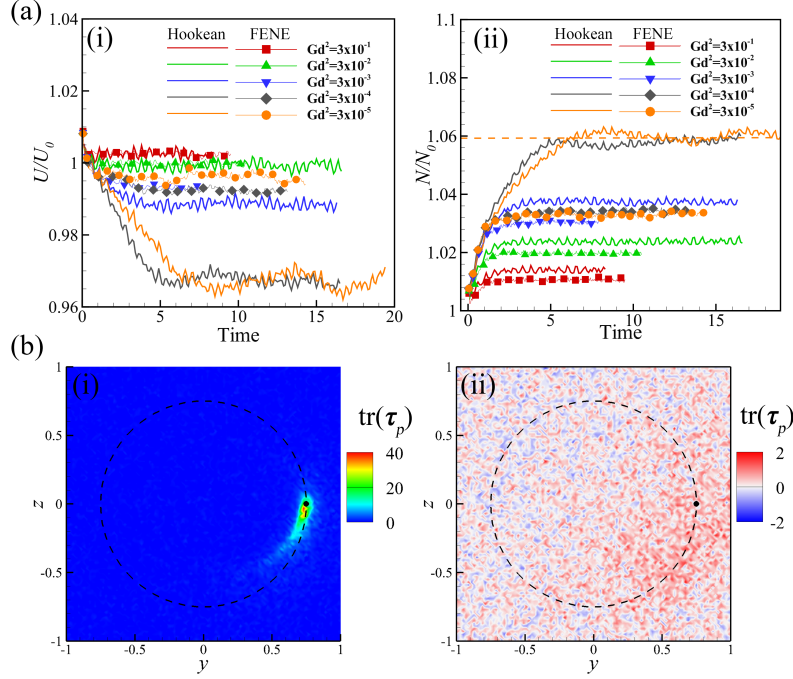


FIG. 7. (a) The temporal evolution of (i) swimming velocity and (ii) torque of the helix at different Gradient numbers for Hookean and FENE dumbbells at $De = 1.0$. The dashed orange line in (ii) is the torque in an Oldroyd-B fluid. (b) The trace of polymer stresses $tr(\tau_p)$ for FENE dumbbells at $De=1.0$ for (i) $Gd^2 = 3 \times 10^{-5}$ and (ii) $Gd^2 = 3 \times 10^{-1}$. Here, the extensibility parameter for FENE dumbbells is $\tilde{b} = 40$. Other parameters are $\phi = 0.27\pi, \gamma = 0.05$, and $r_f = 10^{-3}$.

IV.2. FENE dumbbells

Hookean dumbbells represent the polymer chains whose end-to-end distance is small compared to their contour length. When the polymer chain is greatly stretched by the ambient flow and its end-to-end distance is comparable to its contour length, the tension in the dumbbell resembles the FENE spring. The kinetics of FENE dumbbells could be approximated by FENE-P constitutive equation [39], which describes the dilute polymer solution with a shear-thinning viscosity.

The temporal evolution of swimming speed U/U_0 and torque N/N_0 for FENE dumbbells at different Gradient numbers are compared with those of Hookean dumbbells in Fig. 7. The quasi-steady state results are included in Fig. 5(a). At low Gd , the FENE dumbbells increase the swimming speed and reduce the torque acting on the flagellum, exhibiting a shear-thinning viscosity. However, when Gd is large, the difference between the FENE and Hookean dumbbells is relatively small, and both of them approach the results in the pure solvent. The mean-squared polymer distension field is shown in Fig. 7(b). At low Gd , FENE dumbbells (Fig. 7(b)(i)) exert smaller elastic stresses than Hookean dumbbells (Fig. 5(a)(i)), but when Gd is large, FENE dumbbells also exert negligible stresses to the fluid (Fig. 7(b)(ii)). For fluid dynamics problems with length scale much larger than the polymer dimension, the finite extensibility of polymer chains is considered as a reason for shear-thinning viscosity. But when the flow length scale is small and Gradient number is very large, the flow non-homogeneity effects become dominant. The polymer molecules are not stretched to their maximum length and the averaged polymer stress is very small.

IV.3. Effects of end-to-end distance of the polymer chains on bacterial cell body

The hydrodynamics of a bacterial cell body in the polymer solution is also studied. The cell body is modeled as a spheroid with a major semi-axis $b = 1$ in the x-direction and minor semi-axis $a = 0.35$ in y and z directions. In this section, the length of major semi-axis b is used as the characteristic length. Polymer molecules are modeled as Hookean dumbbells and viscosity ratio is set to $\gamma = 0.05$. Two separate simulations are conducted to compute the drag D/D_0 and torque N/N_0 on the cell body. In the first simulation, the torque on a spheroid that rotates around its major semi-axis with a constant angular speed is calculated. Here, we define the Deborah number as the

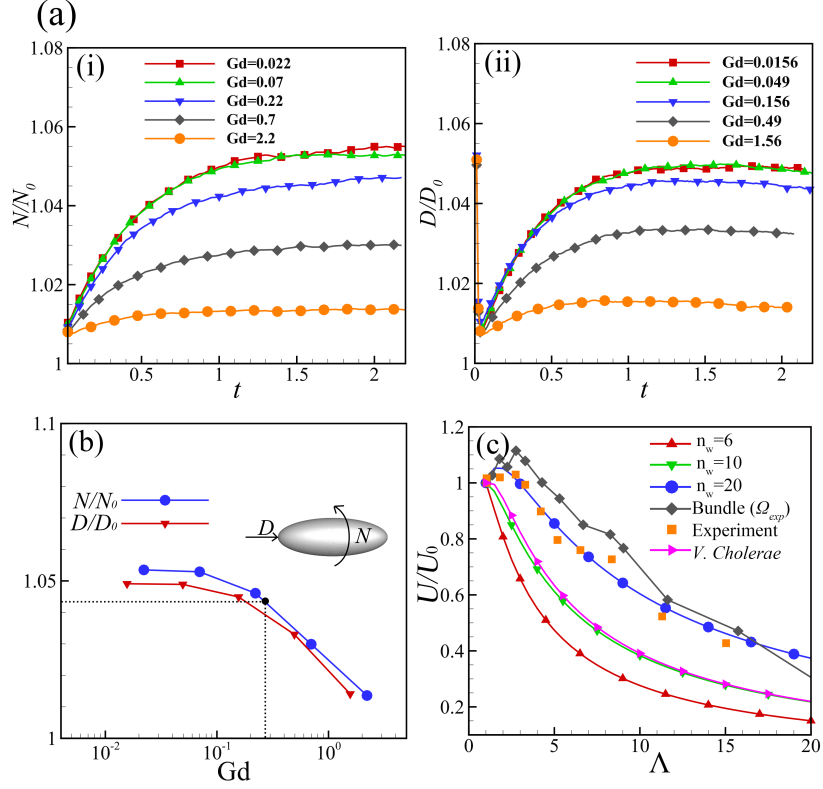


FIG. 8. (a) The temporal evolution of the normalized (i) torque N/N_0 and (ii) drag D/D_0 of the spheroidal cell body at different Gradient numbers. The ratio of minor to major semi-axis of the spheroid is $a/b = 0.35$. (b) The Gradient number dependence of torque N/N_0 and drag D/D_0 . The black dot illustrates the torque for the cell body of *E. coli*. The dimensionless numbers are $De = 0.5$, $Wi = 0.57$ and $\gamma = 0.05$. (c) Polymer concentration dependence of the swimming speed of *E. coli* for different n_w , where n_w is the total number of wavelengths for all the flagella, and $\Lambda = (\eta_s + \eta_p)/\eta_s$ is the viscosity ratio between the polymer solution and the solvent. The orange squares are the experimental data by Martinez *et al.* [20] for *E. coli*. The optimal viscosity of the polymer solution Λ_c is proportional to n_w .

polymer relaxation time over the characteristic time of rotational motion $De = \lambda_H \Omega$, which is 0.5. The domain size is $4 \times 10 \times 10$ and is resolved using $64 \times 90 \times 90$ grid points with two mesh patterns. Inside a middle block of $4 \times 5 \times 5$, grids are uniform with a spacing of $\Delta x = \Delta y = \Delta z = 1/16$. Outside this block the grid spacing is elongated in y and z directions. A periodic boundary condition is applied in the x-direction, and in y and z directions, the velocity gradient is set to zero. The Newtonian torque N_0 over $\eta_s \Omega$, corresponding to \hat{d}_0 , calculated from the simulation is $16.90a^2b$. The error compared to the theoretical results given by the Purcell's model in the next section is 0.9%.

The drag is then evaluated for a spheroid moving with a constant speed along the x-direction. The domain size is $12 \times 5 \times 5$ and is resolved using $120 \times 120 \times 120$ grid points with two mesh patterns. Inside a middle block of $5.14 \times 1.8 \times 1.8$, the grid spacing is $\Delta x = 0.0514$, and $\Delta y = \Delta z = 0.018$. The grid outside this block is coarse and resolved using the remaining grid points. The velocity gradient is set to zero on boundaries in the x-direction. No slip boundary conditions are applied on y and z directions. The Weissenberg number is defined as the polymer relaxation time over the characteristic time of translational motion $Wi = \lambda_H U/a = 0.57$. The time is scaled by U/a . The Newtonian drag D_0 over $\eta_s U$, corresponding to \hat{a}_0 , is $10.37b$. The error from the theoretical results is 2.5%.

In the BD simulations of the spheroid, a bounce-back boundary condition is employed to avoid the penetration of beads into the spheroid. A collision displacement $dr_{c,i} = 2n_{bnd}d$ is added to Eq. (8), where d is the distance the beads penetrate into the body in the previous iteration and n_{bnd} is the local normal vector to the surface of the spheroid, pointing towards the fluid domain.

Fig. 8(a) shows the transient results of the drag and torque acting on the cell body for different Gradient numbers, which is defined as $Gd = \sqrt{\langle Q^2 \rangle_0}/a$. The quasi-steady state results are shown in Fig. 8(b). Here, the torque and drag acting on a spheroidal cell body also decrease with the Gradient number as Gd exceeds a threshold. The critical Gd is larger than that for the flagellum because the length scale over which the flow velocity gradient changes near the flagella is smaller than that near the cell body. For the cell body of *E. coli* (diameter $\sim 1\mu\text{m}$ [40]), the Gradient

number is approximately 0.27. The torque at this Gd is illustrated by the black dotted line in the figure, and the reduction of microscopic viscosity here is relatively small.

IV.4. Applying the resistive force theory and its implication to the bacterial swimming speed

The BD simulation results suggest that the locomotion of the bacterial flagellum resembles that in the solvent. The polymer stresses are effective at the cell body but the Deborah number here is relatively small. Therefore, we approximate the fluid at both the flagellum and the cell body as a Newtonian fluid but of different viscosity: viscosity experienced by the cell body is $\eta_s + \eta_p$ and the viscosity experienced by the flagellum is the solvent viscosity η_s . These assumptions allow us to use the Purcell's model [41–43] to calculate the swimming velocity of a bacterium that consists of a helical flagellum and a cell body. The motion of the bacterium is described by three kinematic parameters: the translational speed of the bacterium U , the angular speed of the flagellum ω and the angular speed of the cell body Ω , whose direction is opposite to ω . The local drag of a segment of the flagellum is $\mathbf{f} = -\xi_t v_t \hat{\mathbf{t}} - \xi_n v_n \hat{\mathbf{n}}$, where ξ is the resistive coefficient and is proportional to the local viscosity. The ratio between the resistive coefficient and the viscosity is defined as $k = \xi/\eta$. Here, v is the local velocity of the filament, subscripts t and n denote the tangential and normal directions to the filament. The ratio between the two drag coefficients is $k^* = \xi_n/\xi_t = k_n/k_t$. The drag force and torque (\mathbb{F}, \mathbb{N}) acting on the flagellum are

$$\begin{pmatrix} \mathbb{F} \\ \mathbb{N} \end{pmatrix} = \eta_f \begin{pmatrix} \hat{a} & -\hat{b} \\ -\hat{b} & \hat{d} \end{pmatrix} \begin{pmatrix} U \\ \omega \end{pmatrix}, \quad (17)$$

where

$$\hat{a} = k_t n_w \lambda \sin \phi \tan \phi (k^* + \cot^2 \phi), \quad (18)$$

$$\hat{b} = k_t n_w \lambda \left(\frac{\lambda}{2\pi} \right) \sin \phi \tan \phi (k^* - 1), \quad (19)$$

$$\hat{d} = k_t n_w \lambda \left(\frac{\lambda}{2\pi} \right)^2 \sin \phi \tan \phi (k^* + \tan^2 \phi), \quad (20)$$

$$k_n = \frac{8\pi}{2 \ln(c' \lambda / r_f) + 1}, \quad (21)$$

$$k_t = \frac{4\pi}{2 \ln(c' \lambda / r_f) - 1}. \quad (22)$$

Here, η_f is the viscosity near the flagellum, n_w is the number of flagellar wavelengths, $\lambda = 2\pi \cos \phi / k$ is the pitch, r_f is the radius of the flagellum filaments and $c' = 2$ is the Lighthill constant [44]. For a very thin flagellum, $k^* \approx 2$. The bacterium *E. coli* has a pitch angle of $\phi \approx 0.23\pi$, pitch of $\lambda \approx 2.5 \cos(\phi) \mu\text{m}$, and radius of filament is $r_f = 0.01 \mu\text{m}$. The coefficients are $\hat{a} = 3.8 n_w \mu\text{m}$, $\hat{b} = 0.26 n_w \mu\text{m}^2$, $\hat{d} = 0.28 n_w \mu\text{m}^3$. The solvent viscosity is the water viscosity $\eta_s = 1 \text{ pN} \cdot \mu\text{m}^{-2} \cdot \text{ms}$.

The viscosity experienced by the cell body is larger than that of the flagellum. Their ratio is defined as $\Lambda = \eta_c/\eta_f$, where η_c and η_f are the viscosity experienced by the cell body and the flagellum. For a bacterium, the force and torque on the flagellum are balanced by the force and torque on the cell body

$$\begin{pmatrix} \mathbb{F} \\ \mathbb{N} \end{pmatrix} = \eta_c \begin{pmatrix} -\hat{a}_0 U \\ \hat{d}_0 \Omega \end{pmatrix}, \quad (23)$$

where

$$\hat{a}_0 = \frac{4\pi b}{\ln(2b/a) - 0.5}, \quad (24)$$

$$\hat{d}_0 = \frac{16\pi}{3} a^2 b. \quad (25)$$

For *E. coli*, the cell body has a major semi-axis $a = 1 \mu\text{m}$ and minor semi-axis $b = 0.5 \mu\text{m}$. The corresponding coefficients are $\hat{a}_0 = 14.2 \mu\text{m}$ and $\hat{d}_0 = 4.2 \mu\text{m}^3$. The torque acting on the flagellum is provided by the motor between the flagellum and the cell body, whose angular speed is $\omega_m = \omega + \Omega$. Experiments have repeatedly shown that the torque of the motor displays two regimes: the torque is constant when ω_m is smaller than a critical frequency $\omega_{m,c}$

and then decreases linearly with the motor frequency ω_m when ω_m exceeds $\omega_{m,c}$ [45]. In a dilute polymer solution, the motor rotates fast and the torque should decrease linearly with $\omega_{m,c}$

$$\mathbb{T} = A - B(\omega + \Omega), \quad (26)$$

where A and B are constants. In the calculation, $A = 4 \text{ pN}\cdot\mu\text{m}$ and $B = 4.5 \text{ pN}\cdot\mu\text{m}\cdot\text{ms}$ for a motor of *E. Coli.* at 16.2°C . [46]. Combining Eq. (23) and Eq.(17), we get

$$\frac{U}{\Omega} = \frac{\hat{b}\hat{d}_0\Lambda}{\hat{a}_0\hat{d}\Lambda + (\hat{a}\hat{d} - \hat{b}^2)}, \quad (27)$$

$$\frac{\omega}{\Omega} = \frac{(\hat{a} + \hat{a}_0\Lambda)\hat{d}_0\Lambda}{\hat{a}_0\hat{d}\Lambda + (\hat{a}\hat{d} - \hat{b}^2)}. \quad (28)$$

Combining Eq. (26) with Eq. (27) and (28), we get

$$U = \frac{\hat{b}A}{(\hat{a}_0\hat{d}\Lambda + (\hat{a}\hat{d} - \hat{b}^2))(\eta_f + \frac{B}{\hat{a}_0\Lambda}) + B\hat{a}_0\Lambda + B\hat{a}}. \quad (29)$$

Eq. (27) indicates that U/Ω increases with Λ . The result has been used by Martinez *et al.* to successfully predict the experimental results of *E. coli* in high-molecular-weight PVP solutions [20]. Assuming that the viscosity experienced by the flagella is the solvent viscosity η_s and does not change with the polymer concentration, we find from Eq. (29) that the swimming speed increases with Λ first and then decreases after Λ reaches Λ_c , where Λ_c is the viscosity ratio at which the swimming speed reaches its maximum. The expression of Λ_c is

$$\Lambda_c = \frac{\eta_c}{\eta_f} = \sqrt{\frac{(\hat{a}\hat{d} - \hat{b}^2)B}{\hat{a}_0\hat{d}_0(B + \hat{d}\eta_s)}}. \quad (30)$$

The condition for the velocity enhancement is $\Lambda_c > 1$. Λ_c is proportional to the number of flagellar wavelengths n_w and slightly increases with the filament radius r_f and the motor torque constant B . In Fig. 8(c), the bacterial swimming speed for different n_w is compared with the experimental results by Martinez *et al.* [20]. Bacteria generally have 3-5 flagella and each of them consists of 2-4 wavelengths [38]. Bacterial flagella during swimming can bundle or unbundle depending on the direction of motor rotation [47]. When flagella are not bundled, we can assume that the drag and torque of each flagella can be added up together. n_w becomes the total number of wavelengths on all the flagella and its range is from 6 to 20. For large n_w (longer flagella and larger number of flagella), the polymer solution enhances the bacterial motility by reducing the rotation of the bacterial cell body. For a flagella bundle, Magariyama *et al.* [48] measured the ratio between the swimming speed of cell U and the flagellar angular speed ω . Their experimental results suggest that the flagellar bundles are more efficient in propelling the cell than a single flagellum and cannot be modeled as a single flagellum with a larger filament radius. They showed that the experimental results of a flagella bundle are closer to the theoretical results if the flagella in the bundle are considered to propel the cell individually. Thus, large n_w may be applicable to flagellar bundles as well. An alternative approach to calculate the swimming speed of a flagellar bundle is to use the experimental value of cell rotation speed, as performed by Martinez *et al.* [20]. The velocity profile obtained by this method is also shown in Fig. 8(c) as the black line. In this calculation, the flagellar bundle is approximated by a single flagellum with number of wavelengths $n_w = 3.5$ and $r_f = 0.02\mu\text{m}$. Fig. 8(c) also shows the swimming speed for *V. Cholerae*, which has only one flagellum with the number of wavelengths $n_w = 3$. The flagellum has a pitch of $\lambda = 2 \mu\text{m}$ and pitch angle $\phi = 0.286\pi$, the head has a major semi-axis $a = 1.1 \mu\text{m}$ and minor semi-axis $b = 0.3 \mu\text{m}$ [49]. The effects of pili are neglected. The current model predicts that the motility of *V. Cholerae* is reduced in a polymeric solution. When the polymer concentration is very high $\Lambda \rightarrow \infty$, the swimming velocity is proportional to Λ^{-1} , which is consistent with the experimental results that the swimming speed of bacteria is inversely proportional to the viscosity of the polymer solution [10, 50].

V. DISCUSSION

Our theory agrees with the hypothesis proposed by Martinez *et al.* [20] that the viscosity near the flagellum is close to the solvent viscosity and much smaller than that of the cell body, but the viscosity reduction in their theory is attributed to the shear thinning effects. One of the most popular molecular explanation for the shear-thinning viscosity of dilute polymer solution is the finite extensibility of polymer chains. In this case, short polymer chains are more likely to be stretched to their maximum length, exhibiting a stronger shear-thinning viscosity. This is, however,

contradictory to the experimental results that the velocity enhancement occurs only for long polymer chains. From our BD results of FENE dumbbells, we also show that at high Gradient numbers, the FENE dumbbells are not stretched to the maximum length and the viscosity is reduced due to the nonuniform flow field rather than the finite extensibility of FENE dumbbells. In addition, the viscosity reduction caused by the non-homogeneous effects is related to the spacial change of shear rate but not the shear rate. For example, in a simple shear flow, the non-homogeneous effects are absent but the shear rate can be very large.

In the experiments by Patteson *et al.*[25] and the simulations by Balin *et al.*[24], the polymer molecules are observed to be effectively stretched by the bacterial flagellum. Polymer stretching can be quantified by the dimensionless distension $(\langle Q^2 \rangle - \langle Q^2 \rangle_0) / \langle Q^2 \rangle_0$, which is an indicator of elastic effects since it is directly related to the trace of polymer stress and the elastic energy stored in polymer molecules. The dumbbells representing long polymer chains in our simulations are also stretched by the bacterial flagellum, but their dimensionless distension is small due to large equilibrium length.

A chain model is a better representation of polymer molecules than the dumbbell model used in the present study. A bead-spring chain has multiple normal modes that stem from the vibration of the chain segments. The normal modes can be described as dumbbells with different relaxation times and equilibrium lengths [26]. The bend and twist of polymer coils can also be incorporated into the chain models by including an angular spring between bonds. For higher concentration polymer solutions, the interaction between polymer molecules becomes important and affects the propulsion of microorganisms.

Our BD simulations extend the study of biolocomotion in the presence of the polymer molecules to include the effects of nanoscopic non-homogeneity across the polymer molecule, i.e., the flow shear rate over the length of polymer chains is dependent on the polymer position and length. The results reveal that when the length scale over which the flow velocity gradient changes is comparable to the radius of gyration of polymer molecules, the Brownian motion of the polymer molecules becomes dominant and both the polymer viscous and elastic stresses decrease. The viscosity experienced by the flagellum asymptotically drops to the solvent viscosity. The theory successfully explains why the velocity enhancement only occurs for long or unbranched polymer solutions, and why the swimming speed of bacteria has a non-monotonic relationship with the polymer concentration. Additionally, since the Gradient number increases with the temperature, our theory suggests that an increase in temperature can reduce the nanoscopic viscosity near the flagellum, potentially changing the swimming speed of bacteria.

-
- [1] G. Taylor, "Analysis of the swimming of microscopic organisms," *Proc. R. Soc. A* **209**, 447–461 (1951).
- [2] E. Lauga and Thomas R. P., "The hydrodynamics of swimming microorganisms," *Rep. Prog. Phys.* **72** (2009).
- [3] E. Lauga, "Bacterial hydrodynamics," *Annu. Rev. Fluid Mech.* **48**, 105–130 (2016).
- [4] C. Datt, G. Natale, S.G. Hatzikiriakos, and G.J. Elfring, "An active particle in a complex fluid," *J. Fluid Mech.* **823**, 675–688 (2017).
- [5] S. Suarez and A. Pacey, "Sperm transport in the female reproductive tract," *Hum. Reprod. Update* **12**, 23–37 (2006).
- [6] S. Jung, "Caenorhabditis elegans swimming in a saturated particulate system," *Phys. Fluids* **22**, 031903 (2010).
- [7] J. P. Celli, B. S. Turner, N. H. Afdhal, S. Keates, I. Ghiran, C. P. Kelly, R. H. Ewoldt, G. H. McKinley, P. So, S. Erramilli, *et al.*, "Helicobacter pylori moves through mucus by reducing mucin viscoelasticity," *Proc. Natl. Acad. Sci. U.S.A.* **106**, 14321–14326 (2009).
- [8] R. B. Kimsey and A. Spielman, "Motility of lyme disease spirochetes in fluids as viscous as the extracellular matrix," *J. Infect. Dis.* **162**, 1205–1208 (1990).
- [9] J.G. Shoemith, "The measurement of bacterial motility," *Microbiology* **22**, 528–535 (1960).
- [10] W. R. Schneider and R.N. Doetsch, "Effect of viscosity on bacterial motility," *J. Bacteriol.* **117**, 696–701 (1974).
- [11] H. C. Fu, C. W. Wolgemuth, and T. R. Powers, "Swimming speeds of filaments in nonlinearly viscoelastic fluids," *Phys. Fluids* **21**, 033102 (2009).
- [12] B. Liu, T. R. Powers, and K. S. Breuer, "Force-free swimming of a model helical flagellum in viscoelastic fluids," *Proc. Natl. Acad. Sci. U.S.A.* **108**, 19516–19520 (2011).
- [13] S. E. Spagnolie, B. Liu, and T. R. Powers, "Locomotion of helical bodies in viscoelastic fluids: Enhanced swimming at large helical amplitudes," *Phys. Rev. Lett.* **111**, 068101 (2013).
- [14] S. Gómez, F. A. Godínez, E. Lauga, and R. Zenit, "Helical propulsion in shear-thinning fluids," *J. Fluid Mech.* **812** (2017).
- [15] G. Li and A.M. Ardekani, "Undulatory swimming in non-Newtonian fluids," *J. Fluid Mech.* **784** (2015).
- [16] E. Lauga, "Propulsion in a viscoelastic fluid. physics of fluids," *Phys. Fluids* **19** (2007).
- [17] H. C. Fu, T. R. Powers, and C. W. Wolgemuth, "Theory of swimming filaments in viscoelastic media," *Phys. Rev. Lett.* **99**, 258101 (2007).
- [18] J. Teran, L. Fauci, and M. Shelley, "Viscoelastic fluid response can increase the speed and efficiency of a free swimmer," *Phys. Rev. Lett.* **104**, 038101 (2010).
- [19] B. Thomases and R. D. Guy, "Mechanisms of elastic enhancement and hindrance for finite-length undulatory swimmers in viscoelastic fluids," *Phys. Rev. Lett.* **113**, 098102 (2014).

- [20] V. A. Martinez, J. Schwarz-Linek, M. Reufer, L. G. Wilson, A. N. Morozov, and W. C. K. Poon, “Flagellated bacterial motility in polymer solutions,” *Proc. Natl. Acad. Sci. U.S.A.* **111**, 17771–17776 (2014).
- [21] H. C. Berg and L. Turner, “Movement of microorganisms in viscous environments,” *Nature* **278**, 349–351 (1979).
- [22] Y. Magariyama, S. Sugiyama, K. Muramoto, I. Kawagishi, Y. Imae, and S. Kudo, “Simultaneous measurement of bacterial flagellar rotation rate and swimming speed,” *Biophys. J.* **69**, 2154–2162 (1995).
- [23] A.M. Leshansky, “Enhanced low-Reynolds-number propulsion in heterogeneous viscous environments,” *Phys. Rev. E* **80**, 051911 (2009).
- [24] A. K. Balin, A. Zöttl, J. M. Yeomans, and T. N. Shendruk, “Biopolymer dynamics driven by helical flagella,” *Phys. Rev. Fluids* **2**, 113102 (2017).
- [25] A.E. Patteson, A. Gopinath, M. Goulian, and P.E. Arratia, “Running and tumbling with e. coli in polymeric solutions,” *Sci. Rep.* **5** (2015).
- [26] B. Bird, *Dynamics of polymeric liquids: Kinetic Theory* (Wiley, 1987).
- [27] A. V. Bhave, R. C. Armstrong, and R. A. Brown, “Kinetic theory and rheology of dilute, nonhomogeneous polymer solutions,” *J. Chem. Phys.* **95**, 2988–3000 (1991).
- [28] G. Li and A. M. Ardekani, “Hydrodynamic interaction of microswimmers near a wall,” *Phys. Rev. E* **90**, 013010 (2014).
- [29] A. M. Ardekani, S. Dabiri, and R. H. Rangel, “Collision of multi-particle and general shape objects in a viscous fluid,” *J. Comput. Phys.* **227**, 10094–10107 (2008).
- [30] P. Pranay, R. G. Henríquez-Rivera, and M. D. Graham, “Depletion layer formation in suspensions of elastic capsules in Newtonian and viscoelastic fluids,” *Phys. Fluids* **24**, 061902 (2012).
- [31] M. Laso and H.C. Öttinger, “Calculation of viscoelastic flow using molecular models: the connffessit approach,” *J. Non-Newtonian Fluid Mech.* **47**, 1–20 (1993).
- [32] G. Tryggvason, B. Bunner, A. Esmaeeli, D. Juric, N. Al-Rawahi, W. Tauber, J. Han, S. Nas, and Y.-J. Jan, “A front-tracking method for the computations of multiphase flow,” *J. Comput. Phys.* **169**, 708–759 (2001).
- [33] G. Li, A. Karimi, and A.M. Ardekani, “Effect of solid boundaries on swimming dynamics of microorganisms in a viscoelastic fluid,” *Rheol. Acta* **53**, 911–926 (2014).
- [34] H. Rezvantlab, G. Zhu, and R. G. Larson, “The effect of wall depletion and hydrodynamic interactions on stress-gradient-induced polymer migration,” *Soft Matter* **12**, 5883–5897 (2016).
- [35] R. Guénette and M. Fortin, “A new mixed finite element method for computing viscoelastic flows,” *J. Non-Newtonian Fluid Mech.* **60**, 27–52 (1995).
- [36] J.W. Rudisill and P.T. Cummings, “Brownian dynamics simulation of model polymer fluids in shear flow. i. dumbbell models,” *J. Non-Newtonian Fluid Mech.* **41**, 275–288 (1992).
- [37] B. Bird, “Polymer solution rheology based on a finitely extensible bead-spring chain model,” *J. Non-Newtonian Fluid Mech.* **7**, 213–235 (1980).
- [38] L. Turner, W. S. Ryu, and H. C. Berg, “Real-time imaging of fluorescent flagellar filaments,” *J. Bacteriol.* **182**, 2793–2801 (2000).
- [39] R.G. Larson and P. S. Desai, “Modeling the rheology of polymer melts and solutions,” *Annu. Rev. Fluid Mech.* **47**, 47–65 (2015).
- [40] D. E. Nelson and K. D. Young, “Penicillin binding protein 5 affects cell diameter, contour, and morphology of escherichia coli,” *J. Bacteriol.* **182**, 1714–1721 (2000).
- [41] E. M. Purcell, “The efficiency of propulsion by a rotating flagellum,” *Proc. Natl. Acad. Sci. U.S.A.* **94**, 11307–11311 (1997).
- [42] S. Chattopadhyay, R. Moldovan, C. Yeung, and X. Wu, “Swimming efficiency of bacterium escherichiacoli,” *Proc. Natl. Acad. Sci. U.S.A.* **103**, 13712–13717 (2006).
- [43] O. S. Pak and E. Lauga, “Theoretical models of low-Reynolds-number locomotion,” in *Fluid-Structure Interactions in Low-Reynolds-Number Flows* (Royal Society of Chemistry, 2015) pp. 100–167.
- [44] J. Gray and G.J. Hancock, “The propulsion of sea-urchin spermatozoa,” *J. Exp. Biol.* **32**, 802–814 (1955).
- [45] Y. Sowa and R. M. Berry, “Bacterial flagellar motor,” *Q. Rev. Biophys.* **41**, 103–132 (2008).
- [46] H. C. Berg and Linda T., “Torque generated by the flagellar motor of Escherichia coli,” *Biophys. J.* **65**, 2201–2216 (1993).
- [47] M. Kim, J. C. Bird, A. J. Van Parys, K. S. Breuer, and T. R. Powers, “A macroscopic scale model of bacterial flagellar bundling,” *Proc. Natl. Acad. Sci. U.S.A.* **100**, 15481–15485 (2003).
- [48] Y. Magariyama, S. Shigeru, and K. Seishi, “Bacterial swimming speed and rotation rate of bundled flagella,” *FEMS Microbiol. Lett.* **199**, 125–129 (2001).
- [49] A. S. Utada, R. R. Bennett, J. C.N. Fong, M. L. Gibiansky, F. H. Yildiz, R. Golestanian, and G. C.L. Wong, “Vibrio cholerae use pili and flagella synergistically to effect motility switching and conditional surface attachment,” *Nat. Commun.* **5**, 4913 (2014).
- [50] H. C. Berg and R. A. Anderson, “Bacteria swim by rotating their flagellar filaments,” *Nature* **245**, 380 – 382 (1973).